A Systematic Search for Lensed High-Redshift Galaxies in HST Images of MACS Clusters

A. Repp[1], H. Ebeling[1], and J. Richard[2]

[1]*Institute for Astronomy, 2680 Woodlawn Dr., Honolulu, Hawaii 96822, USA*
[2]*CRAL, Observatoire de Lyon, Université Lyon 1, 9 Avenue Ch. André, 69561 Saint Genis Laval Cedex, France*

20 December 2016

ABSTRACT
We present the results of a 135-arcmin^2 search for high-redshift galaxies lensed by 29 clusters from the MAssive Cluster and extended MAssive Cluster Surveys (MACS and eMACS). We use relatively shallow images obtained with the Hubble Space Telescope in four passbands, namely, F606W, F814W, F110W, and F140W. We identify 130 F814W dropouts as candidates for galaxies at $z \gtrsim 6$. In order to fit the available broad-band photometry to galaxy spectral energy distribution (SED) templates, we develop a prior for the level of dust extinction at various redshifts. We also investigate the systematic biases incurred by the use of SED-fit software. The fits we obtain yield an estimate of 20 Lyman-break galaxies with photometric redshifts from $z \sim 7$ to 9. In addition, our survey has identified over 100 candidates with a significant probability of being lower-redshift ($z \sim 2$) interlopers. We conclude that even as few as four broad-band filters – when combined with fitting the SEDs – are capable of isolating promising objects. Such surveys thus allow one both to probe the bright end ($M_{1500} \lesssim -19$) of the high-redshift UV luminosity function and to identify candidate massive evolved galaxies at lower redshifts.

Key words: galaxies: high-redshift – galaxies: statistics.

1 INTRODUCTION

Reionization and galaxy formation are key events in cosmic history; the former depends upon, and the latter is responsible for, the characteristics of high-redshift galaxies. Therefore the study of such galaxies is a major component of the ongoing intensive investigation into the early epochs of the universe.

The most credible redshift determinations arise from spectroscopic analysis. Although the catalog of spectroscopically confirmed high-redshift galaxies contines to expand (e.g., Richard et al. 2011; Vanzella et al. 2011; Bradač et al. 2012; Bradley et al. 2012; Ono et al. 2012; Finkelstein et al. 2013, Oesch et al. 2015; Zitrin et al. 2015), the time required to obtain spectra of faint objects limits the scope of spectroscopic surveys. Hence the most fruitful method for expanding the catalog of high-redshift galaxies is the dropout technique (Steidel et al. 1995, 1996), which relies on multiple-passband photometry. Breaks in an object's spectrum – in particular, both the Lyman break (at restframe 912 Å) and the 4000-Å break – can cause it to 'drop out' of passbands blueward of the break due to absorption of its radiation by neutral gas. Comparison of the observed and rest-frame wavelengths of the break immediately yields a crude ('photometric') redshift estimate. One can subsequently improve this estimate by fitting galaxy template spectral energy distributions (SEDs) to the observed multi-band photometry.

Multiple researchers have applied this technique to identify both intermediate-redshift (Steidel et al. 1999; Ellis et al. 2001; Gi-avalisco et al. 2004; Ouchi et al. 2004; Stark et al. 2009; Oesch et al. 2010) and high-redshift galaxies (Beckwith et al. 2006; Bouwens et al. 2006, 2010, 2011; Lorenzoni et al. 2013; Oesch et al. 2013; Schenker et al. 2013; Ellis et al. 2013). The widest of these surveys have covered up to 1.65 deg^2 (e.g., Bowler et al. 2014)

To push this technique to fainter magnitudes, other studies have combined it with the power of gravitational lensing (Ellis et al. 2001; Richard et al. 2006, 2008; Bradley et al. 2014; Atek et al. 2014; Zheng et al. 2014); it was thus that Coe et al. (2013) identified a galaxy with photometric redshift $z \sim 11$ (see also Pirzkal et al. 2015). Lensed surveys tend to cover a smaller solid angle than field surveys because of their dependence on high-mass foreground galaxy clusters. One of the most extensive such projects is the Cluster Lensing And Supernova survey with Hubble (CLASH—Postman et al. 2012), which imaged 25 clusters in 16 filters, with integration times in each filter ranging from 1975 to 4920 s. (See for instance Bradley et al. 2014; Zitrin et al. 2013; Bouwens et al. 2014.) Most lensed surveys apply more time to smaller solid angles; for instance, the Hubble Frontier Fields[1] program devotes 140 orbits to each of six massive clusters. Still ongoing, this deep-imaging program has already detected a substantial number of high-redshift galaxies (see Atek et al. 2014, 2015; Zheng et al. 2014; McLeod et al. 2015; Ishigaki et al. 2015).

---

[1] `http://www.stsci.edu/hst/campaigns/frontier-fields`

Table 1. Exposure times

| | .... Integration Times .... | | | | Fil-ters | Clus-ters |
	F606W	F814W	F110W	F140W		
This work	1200 s	1440 s	706 s	706 s	4	29
CLASH[a]	1975 s	4103 s	2415 s	2342 s	16	25

[a] CLASH integration times are averages from table 5 of Postman et al. (2012). Actual exposure times vary from cluster to cluster, depending on the quality of previous observations.

Despite these successes, photometric redshifts always contain an element of uncertainty, given the possibility of low-redshift objects mimicking the colours of high-redshift galaxies (Mobasher et al. 2005; Schaerer et al. 2007; Schenker et al. 2012). These low-redshift interlopers may be red stars or galaxies with high equivalent-width emission lines (Atek et al. 2011). Thus in searching for high-redshift dropouts, it is important to analyse passbands blueward of the dropout band in order to detect the flux enhancement due to strong emission lines (like Hα and [OIII]) which would indicate a lower redshift.

To summarize, one can increase the yield of photometric redshift surveys by employment of larger sample sizes, by utilization of gravitational lensing from massive galaxy clusters, and by a judicious choice of passbands. The most massive clusters known to date at $z > 0.3$ are those identified by the MAssive Cluster Survey (MACS) (Ebeling et al. 2001, 2007, 2010; Mann & Ebeling 2012), which systematically catalogued the most X-ray luminous – and hence the most massive – galaxy clusters. In this work we employ the lensing power of 29 such clusters not studied by CLASH, thus conducting one of the broadest lensed dropout searches to date. Table 1 compares this survey to CLASH; despite the longer integration times and the greater number of passbands in CLASH, the similarity in solid angle coverage bodes well for the identification high-redshift candidates by our survey.

Throughout this paper we assume a standard concordance cosmology with $H_0 = 70$ km s^{-1} Mpc^{-1}, $\Omega_m = 0.3$, and $\Omega_\Lambda = 0.7$. We express all magnitudes in the AB system (Oke & Gunn 1983).

2   DATA

This survey analyses Hubble Space Telescope (HST) images of the 28 MACS clusters and one eMACS (extended MACS) cluster (Ebeling et al. 2013) listed in Table 2. This sample comprises all MACS clusters that were not part of CLASH and for which HST images exist in all of the following passbands: F606W and F814W on the Advanced Camera for Surveys (ACS); and F110W and F140W on the Wide Field Camera 3 (WFC3). All images were obtained through HST SNAP-shot programs[2]. The exposure times (identical within each passband across all clusters) appear in Table 1.

The WFC3 field of view (4.65 arcmin^2), being smaller than that of the ACS, determines the 135-arcmin^2 solid angle of this survey.

Table 2. Clusters surveyed, with Milky Way hydrogen column density (in units of 10^{20} cm^{-2}) for estimating extinction

Cluster	n_H	Cluster	n_H
eMACSJ1057.5+5759	0.56	MACSJ1354.6+7715	2.86
MACSJ0140.0−0555	2.85	MACSJ1621.4+3810	1.12
MACSJ0152.5−2852	1.51	MACSJ1652.3+5534	2.33
MACSJ0257.6−2209	2.18	MACSJ1731.6+2252	6.29
MACSJ0451.9+0006	7.23	MACSJ1738.1+6006	3.74
MACSJ0712.3+5931	5.43	MACSJ1752.0+4440	3.06
MACSJ0916.1−0023	3.25	MACSJ2050.7+0123	7.50
MACSJ0947.2+7623	2.22	MACSJ2051.1+0215	8.14
MACSJ1115.2+5320	0.90	MACSJ2135.2−0102	4.27
MACSJ1124.5+4351	2.04	SMACSJ0234.7−5831	3.64
MACSJ1133.2+5008	1.44	SMACSJ0549.3−6205	4.50
MACSJ1142.4+5831	1.77	SMACSJ0600.2−4353	6.24
MACSJ1226.8+2153C	1.87	SMACSJ2031.8−4036	3.91
MACSJ1236.9+6311	1.68	SMACSJ2131.1−4019	3.00
MACSJ1319.9+7003	1.47		

3   ANALYSIS

One result of the opportunistic nature of the SNAP-shot program is that the four images of each cluster are taken at random times dictated by scheduling requirements. As a result the images of a given cluster are not, in general, aligned. In addition, the ACS plate scale is significantly smaller than that of WFC3. In order to facilitate comparison between images in different passbands, we redrizzled all images (using `DrizzlePac`[3]) to the pixel scale and reference frame defined by the F140W image for the relevant cluster.

The presence of low-sensitivity regions ('blobs' – see Dressel 2014) can complicate the analysis of WFC3 images. These artefacts are the result of differential reflectivity of the Channel Select Mechanism Mirror. In several instances (discussed in Section 6) one of these blobs (or another defect) in the F110W image coincides with both a detection in the F140W channel and dropout behaviour in F814W and F606W (see for instance the final row of Fig. 6). In addition, ambient light had contaminated the majority of the F110W image for cluster MACSJ0712.3+5931 (see for instance the fourth and fifth rows of Fig. 5). In both of these situations, only three passbands of usable data are available.

We then stacked the F140W and F110W images and ran `SExtractor` (Bertin & Arnouts 1996) in dual-image mode, using the stacked image for detection. We employed a 12-pixel rectangular annulus for background determination and thus obtained a catalog of objects with isophotal magnitudes in each passband. Our inital catalog of SExtractor results comprise 37,809 records, the flux errors of which we corrected for correlated noise according to the prescription of Casertano et al. (2000). Since the WFC3 images determine our segmentation, and since the WFC3 point-spread function (PSF) is significantly wider than that of the ACS, we do not perform any PSF-matching. We want to capture as much flux as possible from the ACS images in order to insure that the objects we consider are truly dropping out in the ACS bands. By retaining the tighter ACS PSF we allow for more accurate detection of this dropout behavior.

The next task is to discriminate between galaxies, stars, and artefacts. To do so, we consider both the objects' morphology and their colours; we describe the morphological criterion here

---

[2] GO-10491, GO-10875, GO-12166, GO-12884: PI H.Ebeling
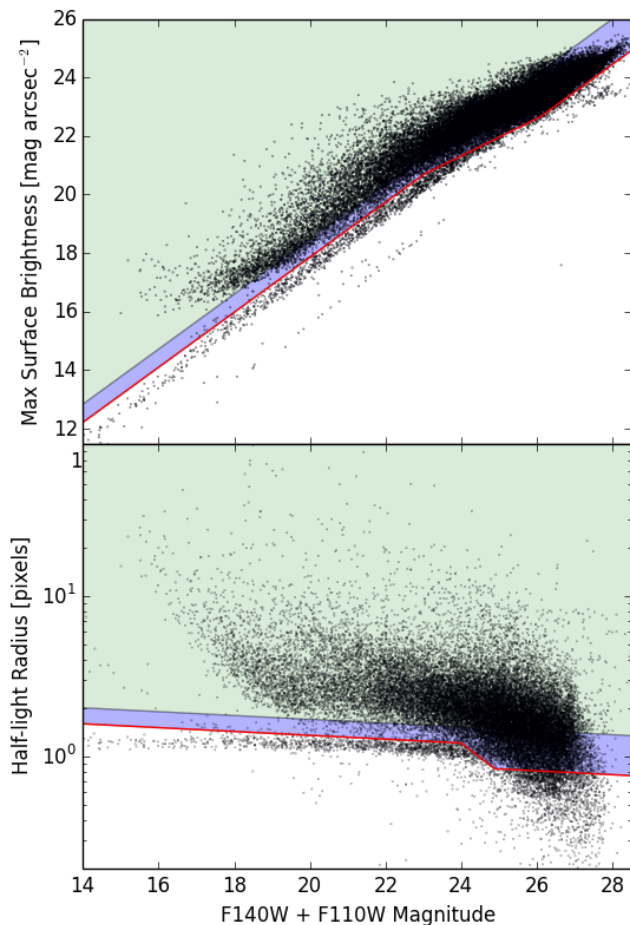
[3] http://drizzlepac.stsci.edu

Figure 1. We use both morphology and spectral energy distribution to discriminate between stars and galaxies; these plots show our morphological criteria. In both panels the line corresponding to point sources (stars) is apparent, running diagonally in the top panel and (roughly) horizontally in the bottom panel. Any object below this line is more compact than a point source and thus must be an artefact. Hence we discard anything in the unshaded portion of either plot. Since the star line and the galaxy cloud begin to interpenetrate at higher magnitudes and since HST may not resolve compact faint high-redshift galaxies, we place this cutoff 1σ above the star line at low magnitudes and 2σ below the star line at high magnitudes. Any object in the light green (upper) region of both plots (3σ above the star line) we accept as a galaxy without further examination. The remaining objects (in the middle, blue-shaded region) we subject to the spectral criterion outlined in Section 4.2.

and the spectral criterion in Section 4.2. As Fig. 1 shows, point sources (stars) occupy a well-defined region ('star line') in both magnitude/surface brightness space and magnitude/half-light radius space. Any object which lies more than 3σ above this line in both plots (i.e., in the light green regions of both panels of Fig. 1) we accept as a galaxy without further examination.

Ideally we could now reject anything on this line as a star and anything below this line as an artefact. However, at higher magnitudes the galaxies begin to bleed into the star line; in addition, high-redshift galaxies can remain unresolved by WFC3 (Oesch et al. 2010). To account for these facts we place the rejection limit 1σ above the star line at low magnitudes but 2σ below the star line at high magnitudes; anything that lies below this limit in either plot (i.e., in the unshaded region of either panel of Fig. 1) we reject as being either a star or an artefact.

The remaining objects lie in the blue region of the figure; we provisionally admit these objects into the next phase of our analysis but will use the spectral criterion of Section 4.2 to eliminate M-stars and brown dwarfs.

At this point we also exclude detections in the noisy portions of the WFC3 field of view.[4]

We identify F814W dropouts by requiring at least a 5σ detection in either WFC3 band (F140W or F110W) and less than 2σ signal-to-noise ratio in both ACS bands (F814W and F606W). We visually inspected the dropouts, eliminating diffraction spikes and areas in which a nearby bright source had corrupted the SExtractor results; we also eliminated 'detections' that appeared to be serendipitously grouped noise.

In addition, we checked the SExtractor segmentation map for these sources to ensure that SExtractor properly discriminated between the objects themselves and neighboring sources. For cases in which it did not, we set an appropriate aperture for each object and reperformed the photometry in those apertures. In some cases the aperture photometry resulted in at least a 2σ detection in the dropout band, causing us to eliminate these sources from consideration. Our final I_{814}-dropout catalog consists of 130 sources.

Finally, to account for foreground (Milky Way) extinction, we first convert the column densities n_H from Table 2 to values of A_V using the prescription of Güver & Özel (2009) and then apply the Cardelli et al. (1989) law to calculate the extinction in each band.

4 SED FITTING

4.1 Obtaining Redshift Probability Distributions

Both the Lyman break and the 4000-Å break can cause dropout behaviour. Thus, a decrease in F814W flux accompanied by a strong detection in F110W could reflect the 4000-Å break redshifted to $1.5 \lesssim z \lesssim 2$ or the Lyman break redshifted to $7 \lesssim z \lesssim 10$. The lower-redshift objects are likely to be massive, passively-evolving galaxies. These galaxies (at such redshifts) typically are quiescent, extremely compact, and already quite old, with mass densities at least an order of magnitude greater than those of local elliptical galaxies (Toft et al. 2012, 2014). Some of these objects appear to be the cores about which the most massive of today's galaxies were built (van Dokkum et al. 2014). Since evolved $z \sim 2$ galaxies can serve as observational proxies for similar objects at higher redshifts, these interlopers are themselves promising candidates for future study.

However, our primary interest for this work is high-redshift galaxies; thus, to exclude low-redshift objects we fit galaxy template spectral energy distributions (SEDs) to the observed fluxes to obtain photometric redshifts for our candidates.

For this purpose we use BPZ[5] (Bayesian Photometric Redshift: Benítez 2000; Benítez et al. 2004; Coe et al. 2006), which matches an object's SED to known galactic spectral types and produces a probability distribution for the object's redshift.

However, BPZ's default templates do not allow one to include extinction as a separate parameter, although they do empirically reproduce the observed photometry of the wide variety of galaxies

---

[4] We exclude detections within fifteen pixels of the edge of the frame as well as in the defect near the bottom of the detector (dubbed the 'death star' in Dressel 2014), in addition to overexposed regions, defined as any region with a surface brightness of less than 15 magnitudes arcsec^{-2}.
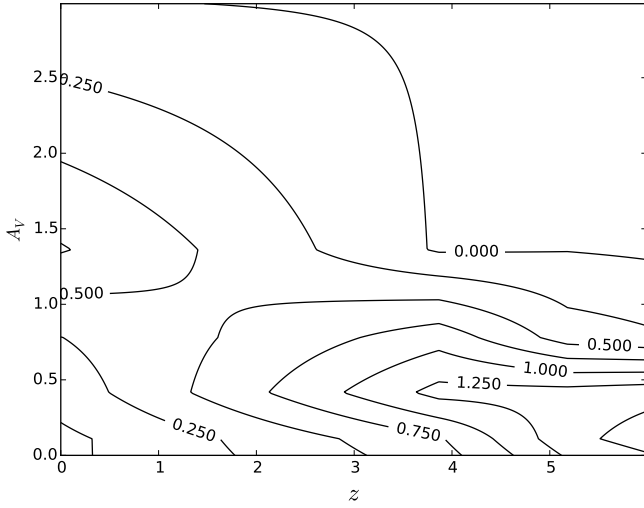
[5] http://www.stsci.edu/~dcoe/BPZ/

Figure 2. Contours showing prior probability distribution for intrinsic extinction A_V at a given redshift z, derived from data in Bouwens et al. (2009) and Magdis et al. (2010).

observed in large-scale surveys (see, for example, Rafelski et al. 2015). We deemed it advisable to explicitly include a prior for intrinsic exinction, given the incidence of galaxies with non-neglible dust attenuation (e.g., Boone et al. 2011; Dey et al. 1999). We thus obtain dust-extinguished templates by applying the Calzetti et al. (2000) extinction law to each default template in increments of $\Delta A_V = 0.5$ from $A_V = 0$ to 3. Not all extinction values occur with equal probability, however, and the probability of extinction evolves with redshift. We therefore require a Bayesian prior for the likelihood of a given extinction A_V at a given redshift. To obtain such a prior we employ the data from fig. 6 of Bouwens et al. (2009), who use observed UV continuum slopes β for a sample of Lyman break galaxies to derive estimates of $E(B-V)$ for redshifts from 2.5 to 6. Bouwens et al. (2009) also estimate the effective selection volume at each redshift, allowing calculation of the percentage of galaxies with a given intrinsic extinction (as a function of redshift). We extend these probabilities to the local universe using Magdis et al. (2010)'s estimate that galaxies are 8 to 10 times less obscured at $z \sim 2$ than they are now; and we extend them to higher redshifts by assuming the same probabilities obtained at $z \sim 6$. We then interpolate, smooth, and normalize the resulting distribution to obtain the prior shown in Fig. 2. One can obtain an analytic estimate for this distribution (Repp and Ebeling, in preparation), but for this work we simply employ the numerical probabilities plotted in the figure.

In addition to the extinction prior, we also require some assumptions about the probability of observing various galactic spectral types at various redshifts. BPZ derives its default $P(z|T)$ prior from the Hubble Ultra-Deep Field; however, since our area is so much larger than that of the HUDF, and since it – by design – includes large-scale structure, one must adopt a broader prior that considers galaxies over a wider range of redshifts and masses than those encountered in the HUDF. In formulating an alternative to the default prior, we must balance the need to rule out inherently improbable results (such as observing an elliptical galaxy at $z = 8$) with our limited knowledge of galaxy evolution.

We first rule out high-redshift ellipticals. We construct a

Schechter luminosity function for elliptical galaxies using the following parameters, derived by Nakamura et al. (2003) from the Sloan Digital Sky Survey (SDSS): $M^*(r^*) = -21.52$; $\alpha = -0.83$; and $\phi^* = 1.61 \times 10^{-3}$ Mpc^{-3}. We then take the BPZ elliptical galaxy template, redshift it, account for intergalactic attenuation (Madau 1995), and convolve it with the F140W filter profile. Thus we derive an apparent magnitude for each combination of absolute magnitude and redshift. By combining this information with our F140W limiting magnitude and the elliptical galaxy luminosity function, we obtain a prior for observing elliptical galaxies which vanishes smoothly around $z = 3.5$.

This constraint on elliptical galaxy visibility follows directly from the weakness of their UV emission combined with their empirically determined maximum luminosities. In recognition of the fact that the luminosity functions evolve with cosmic time (e.g., Bouwens et al. 2011, 2012), we assume flat priors for the other galactic spectral types. In particular, we have modified BPZ so that for each redshift, it reports the goodness-of-fit probability for the *most likely* galaxy template only, rather than summing the probabilities over all templates. (See also the discussion in Section 5.1 concerning comparison of BPZ results with results from hyperz.) Thus we consider only how closely the observed SED fits a galaxy template at high redshift without taking into account the (unknown) likelihood of each template.

To validate the utility of this modification, we next determined which procedure (original or modified BPZ) best reproduces the results of CLASH using only our four passbands. Since CLASH utilizes 16 passbands for their photometric redshift determinations, their multiple bands in essence function as very low-resolution spectroscopy. Thus, reproducing their redshifts would enhance our confidence that our procedure yields reliable results.

We began with 47 high-redshift galaxies from tabs. 5 and 6 of Bradley et al. (2014). For each galaxy, Bradley et al. report the photometric redshift estimate along with the 95 per cent (2σ) confidence interval. We obtained the magnitudes of each galaxy in our four passbands from the CLASH source catalog[6]. We then ran both the original implementation of BPZ and our modified version (using the aforementioned prior on elliptical galaxies in both cases) on these 47 objects using only the four passbands considered in this project. From the BPZ results, we determined the most likely redshifts and 68 per cent (1σ) confidence intervals. Since we only use four passbands whereas CLASH uses 16, we expect their 2σ confidence intervals to be roughly comparable to our 1σ intervals. Our limited number of passbands means that, in many cases, 95 per cent confidence intervals derived from our work would be so broad as to be almost useless. Thus for our own results we quote 68 per cent intervals and, as noted in Section 7, recommend spectroscopic follow-up for our most plausible candidates.

The results appear in Fig. 3. We see that both versions of BPZ, when operating on only four passbands, give highest-likelihood redshifts roughly comparable to those obtained by CLASH. The original version of BPZ, as might be expected, produces a more symmetric scatter about the diagonal $z_{4\text{bands}} = z_{\text{CLASH}}$; it also results in fewer 'catastropic outliers.' However, the results of the modified version are more conservative in that they seldom produce redshifts significantly in excess of the CLASH results. The greatest excess redshift (compared with CLASH) is $\Delta z = 0.5$ for the modified version, as opposed to $\Delta z = 1.5$ for the original version.

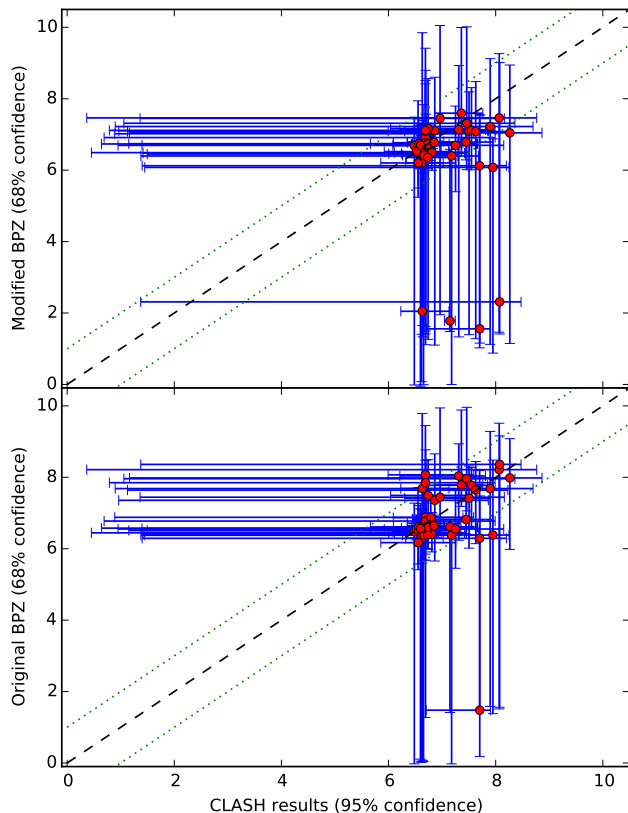In two other respects our approach is conservative: first, we

---

[6] https://archive.stsci.edu/prepds/clash/

Figure 3. Comparison of photometric redshifts derived from CLASH with those derived from four passbands with BPZ (both the original version and as modified – see Section 4). Green dotted lines are $\Delta z = 1$ away from the main diagonal $z_{4\mathrm{bands}} = z_{\mathrm{CLASH}}$. The results of the original BPZ are more symmetric about the diagonal—and have fewer catastrophic outliers. However, the modified version produces more conservative results, in that it is less likely to produce photometric redshifts significantly in excess of the (presumably more nearly correct) CLASH estimates.

apply our extinction prior to all spectral types of galaxies, thus assuming that dusty ellipticals are as likely as dusty starbursts or spirals. Second, we use the SDSS $z = 0$ luminosity function for ellipticals to estimate the likelihood of observing such galaxies at higher redshifts, thus neglecting evolution. As a result of these two assumptions, our estimated likelihood for dusty $z \sim 2$ ellipticals is probably higher than that found in the actual universe. Given our limited number of passbands, our primary concern is to obtain conservative photometric redshifts; we are thus willing to accept results which might underestimate the true redshift. Hence we use the modified version of BPZ, with the understanding that we probably underestimate to some degree the number of galaxies in each high-redshift bin.

4.2 Eliminating Stars and Sub-stellar Objects

Section 3 outlines our two-fold approach to eliminating stars and sub-stellar objects from our list of dropouts. The first aspect of our approach is the morphological criterion displayed in Fig. 1; any objects in the light green portions of this figure we accept as galaxies. However, objects in the blue portions of the figure have ambiguous morphology, and for these objects we use BPZ to determine how well their photometry matches what one would expect for M-stars and brown dwarfs.

To do so, we obtained composite spectra of M-, L-, and T-dwarfs by stacking 25 spectra (Burgasser et al. 2004, 2006; Burgasser 2007a,b; Burgasser et al. 2008, 2010; Chiu et al. 2006; Kirkpatrick et al. 2010) of these objects obtained from the SpeX Prism Spectral Libraries.[7]

We then prepared simulated stellar observations by convolving the model spectra with the HST filter profiles, scaling to magnitudes typical of our candidates and adding uncertainties typical of our candidates. Experimentation showed that, when applied to these simulated stars, BPZ with the extra templates yielded a probability spike at $z = 0$ that was typically at least 30 per cent of the maximum height of the distribution.

Thus, to impose our spectral criterion, we ran BPZ (with the extra templates) on each of our ambiguous candidates and eliminated those for which the probability density at $z = 0$ was at least 30 per cent of the maximum probability density. The remaining objects we retained as galaxies. Finally, we removed the stellar templates from BPZ's template library and re-ran it on these retained objects to obtain the probabilities reported in Table 5 and shown in Figs 5 and 6.

5 DISCUSSION

5.1 SED-fit Codes

There seems to be no 'standard' code for SED-fitting. Bradley et al. (2014) use BPZ, whereas Zheng et al. (2014) use a combination of BPZ and `iSEDfit`. Atek et al. (2014) use `hyperz`; Bowler et al. (2014) use `LePhare`; and Oesch et al. (2013) use `ZEBRA` and `EAZY`. Others (McLure et al. 2011, 2013; Ellis et al. 2013) use proprietary code.

Since there is no accepted best SED-fit code (see Hildebrandt et al. 2010 for a review and evaluation of 17 photometric redshift codes) we thought it useful to compare the results of the two codes with which we are most familiar, namely BPZ (modified as described above) and hyperz[8] (Bolzonella et al. 2000). BPZ marginalizes over a carefully selected set of galaxy templates (a feature which our modification largely circumvents) and naturally accommodates a prior distribution for those templates. It does not naturally handle various levels of intrinsic extinction, requiring us to handle extinction as described in Section 4. On the other hand, hyperz fits not only redshift but also extinction and metallicity; however, it does not seem to accommodate a prior on these variables.

Thus we compare the results of two approaches: the first is a modified BPZ with an extinction prior and a limited galaxy template prior to disallow high-redshift ellipticals; the second is (unmodified) hyperz. The output appears in Fig. 4. We note first the high incidence of objects (blue points) to which the codes assigns a probability distribution which is bimodal at a 68 per cent level (meaning that the 68 per cent confidence region is a topologically disconnected set). The majority of objects for which the 68 per cent BPZ and hyperz results differ (open circles) are these bimodal objects with poorly constrained redshifts. Second, as in the comparison with the CLASH results, we see that our modified version of

---

[7] `http://pono.ucsd.edu/~adam/browndwarfs/`
`spexprism/library.html` We then included these spectra in the BPZ template list and, for these three spectral templates only, imposed a delta-function prior limiting them to $z = 0$.
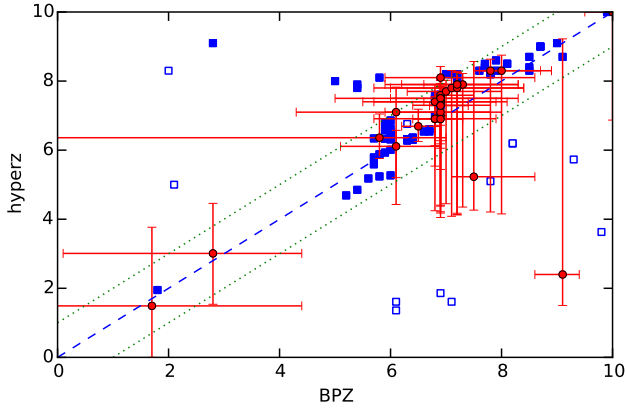[8] `http://webast.ast.obs-mip.fr/hyperz/`

Figure 4. Photometric redshifts produced by BPZ (modified as described in Section 4) and by hyperz. Blue squares indicate probability distributions from BPZ which are bimodal at the 68 per cent level (i.e., the 68 per cent confidence regions are topologically disconnected), with only the most likely redshift plotted for each candidate. Red circles indicate unimodal distributions (connected 68 per cent confidence intervals). Filled markers indicate BPZ results which are consistent (to 68 per cent) with hyperz results; open markers indicate inconsistent results. Dotted lines show a distance of $\Delta z = 1$ from the main diagonal. For readability, we show error bars for consistent and unimodal distributions only. We use only the red data points (redshift probabilities unimodal at 68 per cent) for the remainder of our analysis.

BPZ is conservative in that it tends (with a few exceptions) to assign a *lower* redshift to (unimodal) objects than does hyperz. Thus, consistent with our conservative approach, we shall henceforth ignore all objects to which BPZ assigns a bimodal distribution at the 68 per cent level – i.e., we shall consider only the red points plotted in Fig. 4.

5.2 Magnification

Determining the rest-frame UV magnitude of dropouts requires knowledge of the degree to which gravitational lensing has magnified the object in question. Determination of the lensing magnification requires in turn knowledge of the mass distribution of the foreground cluster.

Mass maps based on spectroscopy of strong-lensing features are available for a fraction of our target clusters, i.e. those for which such features have been spectroscopically confirmed. Magnification estimates were derived by means of Lenstool (Jullo & Kneib 2009) from the positions of strong-lensing features and a parametric model which includes the contribution from cluster-scale and galaxy-scale haloes (following the same approach as, e.g., Richard et al. 2010; Limousin et al. 2015). The available models allowed us to calculate the magnification due to cluster gravity for the ten high-redshift candidates presented in Table 3. Note that the magnification errors include the statistical error from the parametric model but no systematic uncertainties from different modelling approaches. Although the uncertainties listed in Table 3 also include errors propagated from redshift uncertainties, they should thus be regarded as lower limits.

Some of these objects appear to be extremely luminous. Magnitudes below -22 are not unheard of;[9] however, Bouwens et al.

---

[9] An example would be the object at $\alpha = 325.0753169°$, $\delta =$

Table 3. Magnifications obtained for high-redshift candidates

Object ID[a]	Photo-z[b]	Amplification[c]	Nominal M_{1500}[d]
MACSJ0140-0851	$7.6^{+1.0}_{-0.2}$	1.26 ± 0.00	-22.8 ± 0.3
MACSJ0140-1028	$6.1^{+1.4}_{-1.5}$	7.04 ± 1.46	-18.4 ± 0.7
MACSJ0152-0651	$6.7^{+0.4}_{-0.4}$	10.03 ± 0.26	-18.6 ± 0.2
MACSJ0152-0871	$6.9^{+0.1}_{-0.1}$	7.25 ± 0.03	-21.9 ± 0.0
MACSJ0712-0608	$7.0^{+0.8}_{-0.8}$	1.24 ± 0.00	-21.1 ± 0.2
MACSJ0712-0699	$8.0^{+1.9}_{-0.5}$	1.51 ± 0.01	-23.1 ± 0.5
MACSJ0947-0072	$6.5^{+0.4}_{-0.3}$	1.17 ± 0.00	-22.2 ± 0.1
MACSJ1133-0922	$7.2^{+1.1}_{-1.0}$	1.28 ± 0.00	-21.3 ± 0.2
MACSJ2135-0509	$6.9^{+0.7}_{-0.4}$	5.15 ± 0.10	-19.7 ± 0.2
MACSJ2135-0763	$9.1^{+0.3}_{-0.5}$	1.41 ± 0.00	-23.8 ± 0.1

[a] See Table 5.
[b] 68 per cent confidence intervals.
[c] Derived from Lenstool (Jullo & Kneib 2009) models.
[d] Uncertainties propagated from photo-z uncertainties.

(2011) note that UV magnitudes below -24 are physically unlikely, given that the vigorous star formation required for such luminosity would quickly fill the galaxy with dust. One of our objects (MACSJ2135-0763) approaches this limit of -24. One possible explanation is galaxy-galaxy lensing, given the nearby lower-redshift galaxy visible immediately to the left (in the third row of Fig. 6). Another possibility is that the photometric redshift, despite being constrained by BPZ at the 68 per cent level, is in error. Inspection of its redshift probability distribution (Fig. 6) shows a non-negligible probability of $z \sim 2$; nevertheless, the probability of $z \geqslant 6.5$ is around 85 per cent (see Table 5). This object would merit additional investigation.

6   RESULTS

Given our extinction prior, our galaxy type prior, and our modified version of BPZ, we determine both a posterior probability distribution and a best-fitting SED for each of the dropout galaxies. We retain only the 50 objects which meet the following criteria. First, the BPZ-derived probability distribution must peak at $z > 5.5$. Second, the probability distribution must be unimodal at the 68 per cent level; by this we mean that the 68 per cent confidence region (shaded blue in Figs. 5 and 6) must be a connected set, so that only one peak rises to 68 per cent significance. Table 5 lists all 50 of these I_{814}-dropout galaxies, their magnitudes (corrected for Milky Way extinction) in each of the four passbands; their photometric redshifts; and their probabilities of falling into redshift bins $z \sim 7$, $z \sim 8$, and $z \sim 9$.

Note that two of these objects (EMACSJ1057-2279 and EMACSJ1057-2476 in Table 5) appear to be multiply lensed images of the same source. Both of these objects appear in the top row of Fig. 5; the first is in the centre of the stamp; the other is barely visible at the right-hand edge of the stamp. We make no attempt to determine the number of other objects in our sample which might be multiply lensed, and in this work we do not account for

---

$-23.6772512°$ in table 4 of Bradley et al. (2014), which yields a restframe M_{1500} around -23, although the authors note a small possibility that the unresolved source might be a star.

Figure 5. Images (5 arcsec per side), redshift probability distributions, and best-fitting SEDs for selected dropout galaxies. For object IDs see Table 5. Blue shading denotes 68 per cent confidence (also noted above the probability plots). Red SEDs show the most probable fit; grey SEDs show the most probable low-redshift fit. The best-fitting template for each case appears above the SED plot. Green dotted lines show limiting magnitude in each filter.
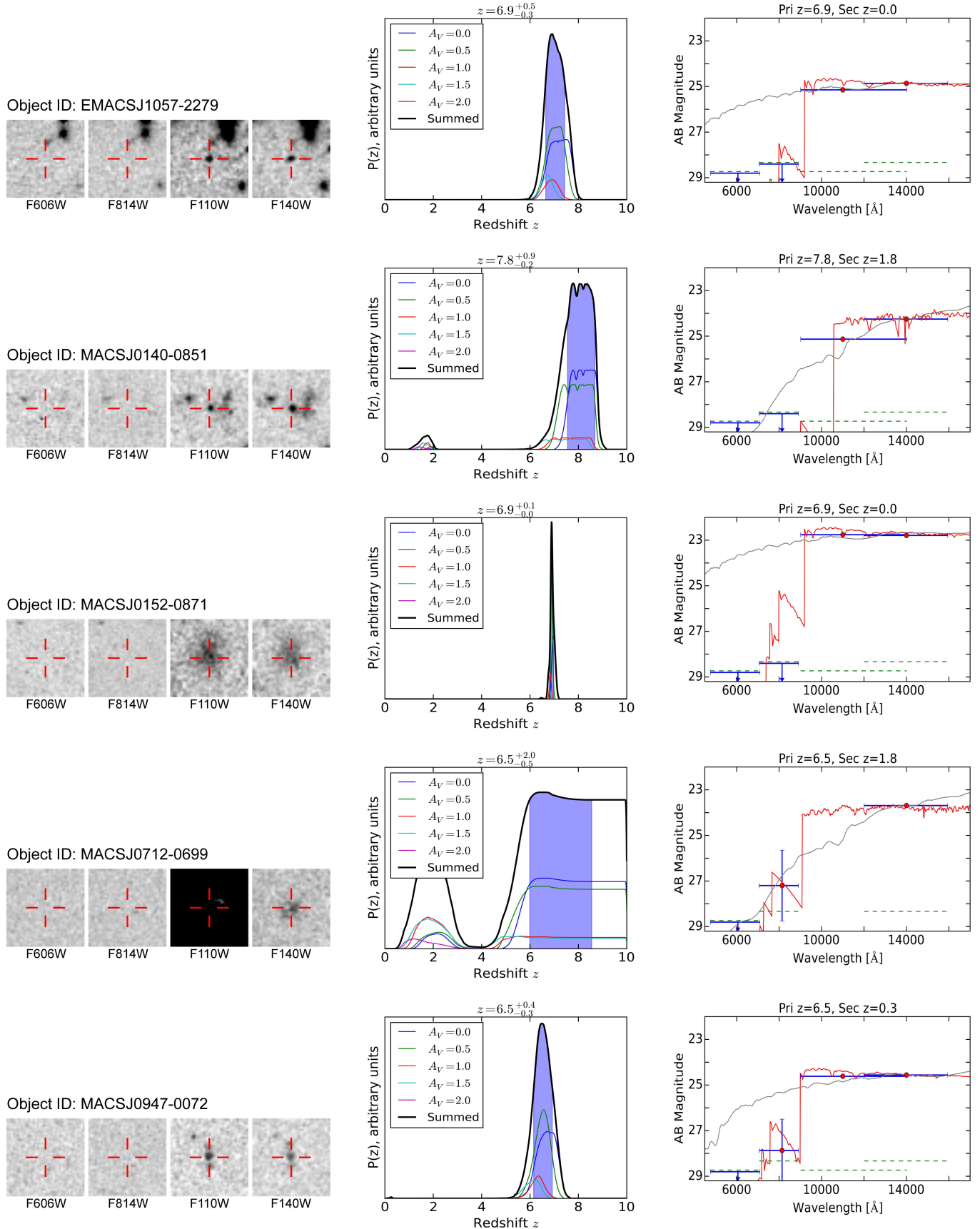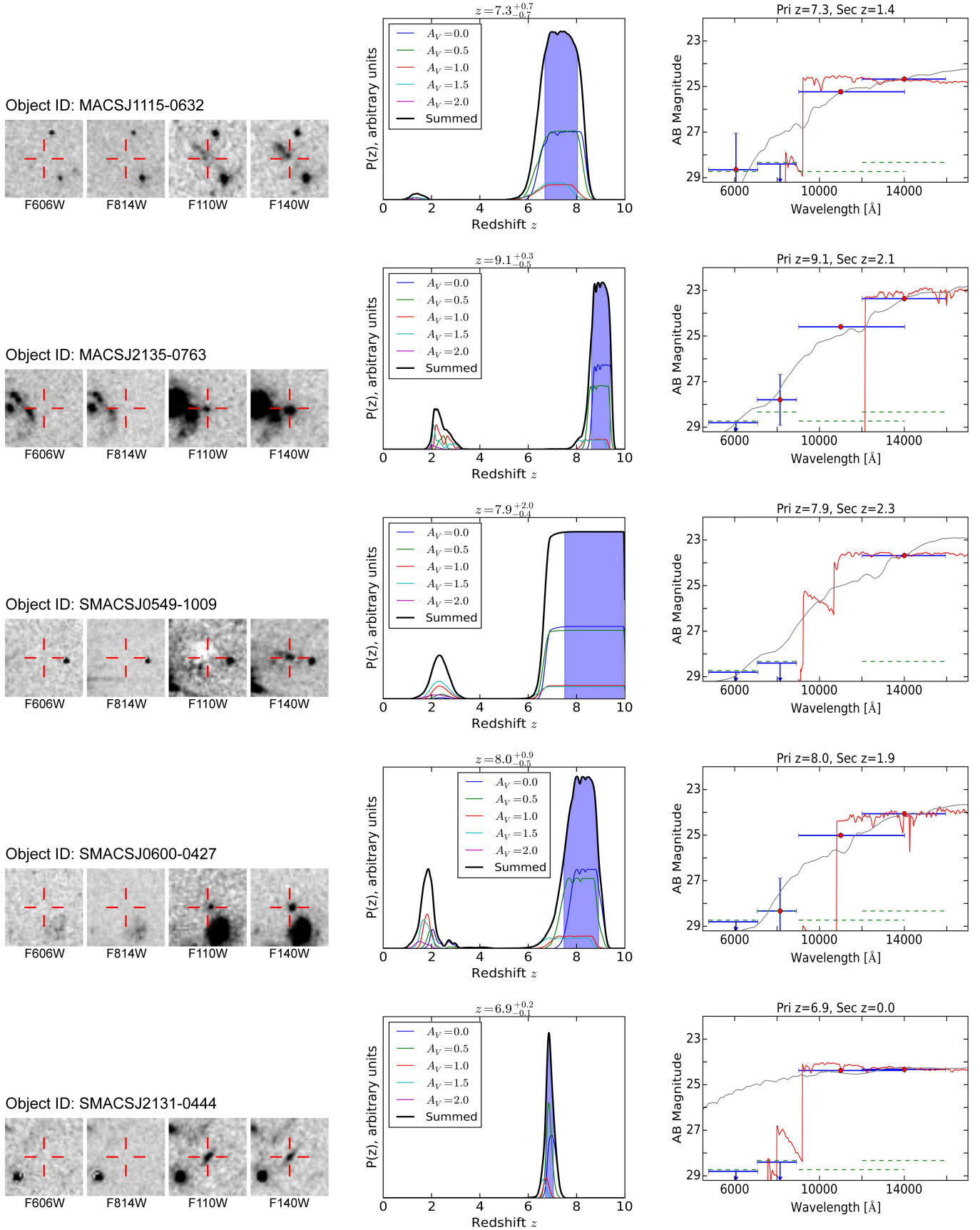
Figure 6. Images (5 arcsec per side), redshift probability distributions, and best-fitting SEDs for selected dropout galaxies. For object IDs see Table 5. Blue shading denotes 68 per cent confidence (also noted above the probability plots). Red SEDs show the most probable fit; grey SEDs show the most probable low-redshift fit. The best-fitting template for each case appears above the SED plot. Green dotted lines show limiting magnitude in each filter.

Table 4. Surveys plotted in Fig. 7

Reference	Survey/Field(s)	Depth[a] (5σ)	Solid Angle (arcmin^2)
Atek et al. (2014)	Abell-2744 (HFF)	28.5	4.7
Bouwens et al. (2011)	HUDF09, ERS	28.5	53
Bouwens et al. (2014)	CLASH	27.4	77
Bradley et al. (2014)	CLASH	27.4	82
Ellis et al. (2013)	HUDF	29.5	4.7
Zheng et al. (2014)	Abell-2744 (HFF)	28.5	4.7
This work	MACS	26.6	135

[a]Limiting magnitude in F140W filter, or interpolated between F125W and F160W limiting magnitudes if F140W not utilized. If depths differ across fields in the same survey, we cite an average depth weighted by the solid angle of the fields involved.
[b]In image plane, not source plane.

this source of systematic error in our sums of objects in each red-shift bin.

The F110W photometry of four of these objects is defective, as noted in Section 3. The objects appear at the end of Table 5; in addition, one of them appears in the fourth row of Fig. 5, and another appears in the fourth row of Fig. 6. For these objects, BPZ yields a relatively flat probability distribution at higher redshifts; in such cases, we weight the probability of galaxies' placement into redshift bins with the summed probabilities for the other dropout galaxies – in essence using the other galaxies' redshifts as a prior for those with defective F110W photometry. Figs. 5 and 6 show the images, probability distributions, and SEDs for some of the galaxies with the greatest likelihood of lying at a high redshift.

By summing the probabilities in Table 5, we obtain the total number of galaxies detected in each bin (also reported in Table 5), which round to 19 galaxies at $z \sim 7$, 6 at $z \sim 8$, and 3 at $z \sim 9$. We thus estimate a total number of 27 high-redshift galaxies, which is one less than the sum of the above numbers due to rounding. (See the table for 68 per cent Poisson confidence intervals.) These sums include one galaxy (MACSJ1319-0075) for which the BPZ confidence interval $z = 9.3^{+0.5}_{-0.7}$ is inconsistent with the hyperz confidence interval $z = 5.7^{+0.6}_{-3.5}$. This object corresponds to the single open red circle in Fig. 4 and appears with a footnote in the table.

Finally, in order to evaluate the effectiveness of our approach, we compare the number of high-redshift galaxies estimated in this survey with those detected by others. One would expect a positive correlation between the number of galaxies and the limiting magnitude of the survey. Using a thousand $0.4''$-diameter apertures in each of our clusters, we determine that the 5σ limiting magnitude for our survey in F140W is 26.6. Normalizing the number of detected high-redshift objects to the solid angle coverage of various searches, and plotting the results against limiting magnitudes, we obtain Fig. 7. (See also Table 4 for the fields involved.)

Note that this figure combines surveys with disparate parameters (e.g., various detection bands, differing uniformity of depth, lensed/unlensed, etc.); thus one ought not to attempt to derive any sort of cumulative luminosity function from it. However, what Fig. 7 does show is that our survey returns a number of galaxies commensurate with our low limiting magnitude. It is the large solid angle of our survey that permits discovery of a non-negligible number of high-redshift candidates, underlining that shallow, wide surveys efficiently probe the bright end of the high-redshift UV luminosity function.
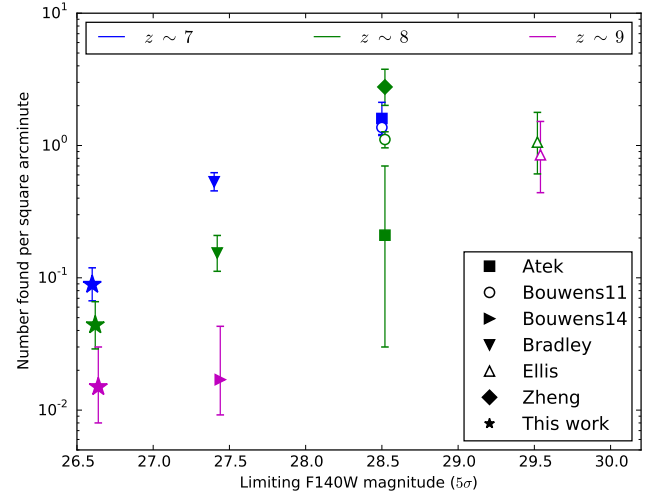

Figure 7. Comparison of the number of objects found in this work to that detected by other surveys, as a function of limiting magnitude. Filled symbols denote lensed surveys, and unfilled symbols denote unlensed surveys. (See Table 4 for details.) Blue markers indicate objects at $z \sim 7$; green, at $z \sim 8$; and magenta, at $z \sim 9$. Markers for $z \sim 8$ and $z \sim 9$ are slightly offset horizontally for clarity. Error bars represent Poisson confidence intervals. Note that for lensed surveys the vertical axis lists the number of objects per unit solid angle in the image plane, not the source plane.

7 CONCLUSIONS

We draw the following conclusions from our survey. First, broad and relatively shallow surveys like ours can effectively detect high-redshift galaxy candidates. Devoting only about an hour of Hubble time to each of 29 clusters, we were able to identify 50 objects which have a probability distribution which peaks at high redshift and is unimodal at the 68 per cent level. Of these objects, we estimate that 27 lie at redshift $z \gtrsim 7$. Since our survey is relatively shallow, we are therefore sampling the bright end of the UV galaxy luminosity function at such redshifts. Our currently available mass maps suggest the existence of several extremely luminous objects with a photometric redshift of $z \sim$ 8–9, placing them only about 600 Myr after decoupling. Such objects are ideal targets for further study, if for no other reason than to confirm or falsify the high photometric redshifts.

This further investigation is important for at least three reasons. First, despite our rejection of objects with significantly bimodal distributions, inspection of Table 5 shows that almost all of the remaining objects still have non-negligible lower-redshift probabilities. Indeed, the summed likelihoods show that we can expect only 27 of the 50 listed objects to actually lie at $z \gtrsim 7$. Second, we derived our extinction prior from Lyman-break galaxy data, whereas low-redshift F814W dropouts represent a different population (4000-Å break galaxies and possibly some high-luminosity infrared galaxies). This population mismatch at lower redshifts could potentially introduce a systematic bias into our results. Third, our analysis of BPZ and hyperz shows that the two codes can occasionally yield wildly divergent results. Thus the choice of a specific SED-fit routine can introduce additional – and probably significant – systematic bias. We are unable to quantify these biases, and the resulting intrinsic uncertainty is not captured in the statistical error bars we report.

We note, however, that the low-redshift interlopers are scientifically interesting in their own right. Over 70 of our 124 F814W-

dropout galaxies do not appear in Table 5 due to bimodalities in their probability distributions; thus, besides high-redshift candidates like those we report in this work, surveys such as ours can identify a large number of lower-redshift objects conducive to the study of galaxy evolution.

Finally, we conclude that even as few as four broad-band filters suffice to isolate promising objects. However, our results also reinforce the importance of SED fitting in obtaining reliable photometric redshifts: dependence on a simple dropout criterion alone would have doubled our catalog size by introducing objects with a significant likelihood of lying at low redshift. SED-fitting is especially important for surveys which utilize a small number of passbands; a greater number of passbands allows the use of more complex colour criteria (e.g., Castellano et al. 2010) which in practice function as a coarse SED fit. In particular, the F606W band was necessary to eliminate high equivalent-width emission-line galaxies from our sample. The small number of passbands did lead to a large number of objects with significantly bimodal photometric redshifts, which we eliminated from consideration; it was the large solid angle of the survey which permitted isolation of a significant number of more securely identified objects.

Spectroscopic investigations of some of our best candidates promise to better constrain these objects' redshifts, as do deeper space-based observations with more filters, and/or slitless near-infrared spectroscopy with WFC3 grisms. In addition, the eMACS SNAPs program proposes to survey 50 massive clusters with $z > 0.5$. Application of our method to this and other future programs has the potential to isolate yet more promising candidates. Thus we confidently expect that the study of high-redshift galaxies will continue to shed light on the processes occurring in the early universe.

REFERENCES

Atek H., Richard J., Kneib J.-P., Clement B., Egami E., Ebeling H., Jauzac M., et al., 2014, ApJ, 786, 60

Atek H., Richard J., Kneib J.-P., Jauzac M., Schaerer D., Clement B., Limousin M., Jullo E., Natarajan P., Egami E., Ebeling H., 2015, ApJ, 800, 18

Atek H., Siana B., Scarlata C., Malkan M., McCarthy P., Teplitz H., Henry A., Colbert J., et al., 2011, ApJ, 743, 121

Beckwith S. V. W., Stiavelli M., Koekemoer A. M., Caldwell J. A. R., Ferguson H. C., Hook R., Lucas R. A., et al., 2006, AJ, 132, 1729

Benítez N., 2000, ApJ, 536, 571

Benítez N., Ford H., Bouwens R., Menanteau F., Blakeslee J., Gronwall C., Illingworth G., et al., 2004, ApJS, 150, 1

Bertin E., Arnouts S., 1996, A&AS, 117, 393

Bolzonella M., Miralles J.-M., Pelló R., 2000, A&A, 363, 476

Boone F., Schaerer D., Pelló R., Lutz D., Weiss A., Egami E., Smail I., et al., 2011, A&A, 534, A124

Bouwens R. J., Bradley L., Zitrin A., Coe D., Franx M., Zheng W., Smit R., et al., 2014, ApJ, 795, 126

Bouwens R. J., Illingworth G. D., Blakeslee J. P., Franx M., 2006, ApJ, 653, 53

Bouwens R. J., Illingworth G. D., Franx M., Chary R.-R., Meurer G. R., Conselice C. J., Ford H., et al., 2009, ApJ, 705, 936

Bouwens R. J., Illingworth G. D., Oesch P. A., Labbé I., Trenti M., van Dokkum P., Franx M., et al., 2011, ApJ, 737, 90

Bouwens R. J., Illingworth G. D., Oesch P. A., Stiavelli M., van Dokkum P., Trenti M., Magee D., et al., 2010, ApJ, 709, L133

Bouwens R. J., Illingworth G. D., Oesch P. A., Trenti M., Labbé I., Franx M., Stiavelli M., et al., 2012, ApJ, 752, L5

Bowler R. A. A., Dunlop J. S., McLure R. J., Rogers A. B., McCracken H. J., Milvang-Jensen B., Furusawa H., et al., 2014, MNRAS, 440, 2810

Bradač M., Vanzella E., Hall N., Treu T., Fontana A., Gonzalez A. H., Clowe D., et al., 2012, ApJ, 755, L7

Bradley L. D., Trenti M., Oesch P. A., Stiavelli M., Treu T., Bouwens R. J., Shull J. M., et al., 2012, ApJ, 760, 108

Bradley L. D., Zitrin A., Coe D., Bouwens R., Postman M., Balestra I., Grillo C., et al., 2014, ApJ, 792, 76

Burgasser A. J., 2007a, ApJ, 659, 655

Burgasser A. J., 2007b, ApJ, 658, 617

Burgasser A. J., Burrows A., Kirkpatrick J. D., 2006, ApJ, 639, 1095

Burgasser A. J., Cruz K. L., Cushing M., Gelino C. R., Looper D. L., Faherty J. K., Kirkpatrick J. D., Reid I. N., 2010, ApJ, 710, 1142

Burgasser A. J., Liu M. C., Ireland M. J., Cruz K. L., Dupuy T. J., 2008, ApJ, 681, 579

Burgasser A. J., McElwain M. W., Kirkpatrick J. D., Cruz K. L., Tinney C. G., Reid I. N., 2004, AJ, 127, 2856

Calzetti D., Armus L., Bohlin R. C., Kinney A. L., Koornneef J., Storchi-Bergmann T., 2000, ApJ, 533, 682

Cardelli J. A., Clayton G. C., Mathis J. S., 1989, ApJ, 345, 245

Casertano S., de Mello D., Dickinson M., Ferguson H. C., Fruchter A. S., Gonzalez-Lopezlira R. A., Heyer I., et al., 2000, AJ, 120, 2747

Castellano M., Fontana A., Boutsia K., Grazian A., Pentericci L., Bouwens R., Dickinson M., et al., 2010, A&A, 511, A20

Chiu K., Fan X., Leggett S. K., Golimowski D. A., Zheng W., Geballe T. R., Schneider D. P., Brinkmann J., 2006, AJ, 131, 2722

Coe D., Benítez N., Sánchez S. F., Jee M., Bouwens R., Ford H., 2006, AJ, 132, 926

Coe D., Zitrin A., Carrasco M., Shu X., Zheng W., Postman M., Bradley L., et al., 2013, ApJ, 762, 32

Dey A., Graham J. R., Ivison R. J., Smail I., Wright G. S., Liu M. C., 1999, ApJ, 519, 610

Dressel L., 2014, Wide Field Camera 3 Instrument Handbook, Version 6.0

Ebeling H., Barrett E., Donovan D., Ma C.-J., Edge A. C., van Speybroeck L., 2007, ApJ, 661, L33

Ebeling H., Edge A. C., Burgett W. S., Chambers K. C., Hodapp K. W., Huber M. E., Kaiser N., Price P. A., Tonry J. L., 2013, MNRAS, 432, 62

Ebeling H., Edge A. C., Henry J. P., 2001, ApJ, 553, 668

Ebeling H., Edge A. C., Mantz A., Barrett E., Henry J. P., Ma C. J., van Speybroeck L., 2010, MNRAS, 407, 83

Ellis R., Santos M. R., Kneib J.-P., Kuijken K., 2001, ApJ, 560, L119

Ellis R. S., McLure R. J., Dunlop J. S., Robertson B. E., Ono Y.,

Schenker M. A., Koekemoer A., et al., 2013, ApJ, 763, L7

Finkelstein S. L., Papovich C., Dickinson M., Song M., Tilvi V., Koekemoer A. M., Finkelstein K. D., et al., 2013, Nature, 502, 524

Giavalisco M., Dickinson M., Ferguson H. C., Ravindranath S., Kretchmer C., Moustakas L. A., Madau P., et al., 2004, ApJ, 600, L103

Güver T., Özel F., 2009, MNRAS, 400, 2050

Hildebrandt H., Arnouts S., Capak P., Moustakas L. A., Wolf C., Abdalla F. B., Assef R. J., et al., 2010, A&A, 523, A31

Ishigaki M., Kawamata R., Ouchi M., Oguri M., Shimasaku K., Ono Y., 2015, ApJ, 799, 12

Jullo E., Kneib J.-P., 2009, MNRAS, 395, 1319

Kirkpatrick J. D., Looper D. L., Burgasser A. J., Schurr S. D., Cutri R. M., Cushing M. C., Cruz K. L., et al., 2010, ApJS, 190, 100

Limousin M., Richard J., Jullo E., Jauzac M., Ebeling H., Bonamigo M., Alavi A., Clement B., et al., 2015, preprint (arXiv:1510.08077)

Lorenzoni S., Bunker A. J., Wilkins S. M., Caruana J., Stanway E. R., Jarvis M. J., 2013, MNRAS, 429, 150

Madau P., 1995, ApJ, 441, 18

Magdis G. E., Elbaz D., Daddi E., Morrison G. E., Dickinson M., Rigopoulou D., et al., 2010, ApJ, 714, 1740

Mann A. W., Ebeling H., 2012, MNRAS, 420, 2120

McLeod D. J., McLure R. J., Dunlop J. S., Robertson B. E., Ellis R. S., Targett T. A., 2015, MNRAS, 450, 3032

McLure R. J., Dunlop J. S., Bowler R. A. A., Curtis-Lake E., Schenker M., Ellis R. S., Robertson B. E., et al., 2013, MNRAS, 432, 2696

McLure R. J., Dunlop J. S., de Ravel L., Cirasuolo M., Ellis R. S., Schenker M., Robertson B. E., et al., 2011, MNRAS, 418, 2074

Mobasher B., Dickinson M., Ferguson H. C., Giavalisco M., Wiklind T., Stark D., Ellis R. S., et al., 2005, ApJ, 635, 832

Nakamura O., Fukugita M., Yasuda N., Loveday J., Brinkmann J., Schneider D. P., et al., 2003, AJ, 125, 1682

Oesch P. A., Bouwens R. J., Illingworth G. D., Carollo C. M., Franx M., Labbé I., Magee D., et al., 2010, ApJ, 709, L16

Oesch P. A., Bouwens R. J., Illingworth G. D., Labbé I., Franx M., van Dokkum P. G., Trenti M., et al., 2013, ApJ, 773, 75

Oesch P. A., van Dokkum P. G., Illingworth G. D., Bouwens R. J., Momcheva I., Holden B., Roberts-Borsani G. W., Smit R., Franx M., Labbé I., González V., Magee D., 2015, ApJ, 804, L30

Oke J. B., Gunn J. E., 1983, ApJ, 266, 713

Ono Y., Ouchi M., Mobasher B., Dickinson M., Penner K., Shimasaku K., Weiner B. J., et al., 2012, ApJ, 744, 83

Ouchi M., Shimasaku K., Okamura S., Furusawa H., Kashikawa N., Ota K., Doi M., et al., 2004, ApJ, 611, 660

Pirzkal N., Coe D., Frye B. L., Brammer G., Moustakas J., Rothberg B., Broadhurst T. J., Bouwens R., Bradley L., van der Wel A., Kelson D. D., Donahue M., Zitrin A., Moustakas L., Barker E., 2015, ApJ, 804, 11

Postman M., Coe D., Benítez N., Bradley L., Broadhurst T., Donahue M., Ford H., others. 2012, ApJS, 199, 25

Rafelski M., Teplitz H. I., Gardner J. P., Coe D., Bond N. A., Koekemoer A. M., Grogin N., Kurczynski P., et al., 2015, AJ, 150, 31

Richard J., Kneib J.-P., Ebeling H., Stark D. P., Egami E., Fiedler A. K., 2011, MNRAS, 414, L31

Richard J., Kneib J.-P., Limousin M., Edge A., Jullo E., 2010, MNRAS, 402, L44

Richard J., Pelló R., Schaerer D., Le Borgne J.-F., Kneib J.-P., 2006, A&A, 456, 861

Richard J., Stark D. P., Ellis R. S., George M. R., Egami E., Kneib J.-P., Smith G. P., 2008, ApJ, 685, 705

Schaerer D., Hempel A., Egami E., Pelló R., Richard J., Le Borgne J.-F., Kneib J.-P., et al., 2007, A&A, 469, 47

Schenker M. A., Robertson B. E., Ellis R. S., Ono Y., McLure R. J., Dunlop J. S., Koekemoer A., et al., 2013, ApJ, 768, 196

Schenker M. A., Stark D. P., Ellis R. S., Robertson B. E., Dunlop J. S., McLure R. J., Kneib J.-P., Richard J., 2012, ApJ, 744, 179

Stark D. P., Ellis R. S., Bunker A., Bundy K., Targett T., Benson A., Lacy M., 2009, ApJ, 697, 1493

Steidel C. C., Adelberger K. L., Giavalisco M., Dickinson M., Pettini M., 1999, ApJ, 519, 1

Steidel C. C., Giavalisco M., Dickinson M., Adelberger K. L., 1996, AJ, 112, 352

Steidel C. C., Pettini M., Hamilton D., 1995, AJ, 110, 2519

Toft S., Gallazzi A., Zirm A., Wold M., Zibetti S., Grillo C., Man A., 2012, ApJ, 754, 3

Toft S., Smolčić V., Magnelli B., Karim A., Zirm A., Michalowski M., Capak P., et al., 2014, ApJ, 782, 68

van Dokkum P. G., Bezanson R., van der Wel A., Nelson E. J., Momcheva I., Skelton R. E., Whitaker K. E., et al., 2014, ApJ, 791, 45

Vanzella E., Pentericci L., Fontana A., Grazian A., Castellano M., Boutsia K., Cristiani S., et al., 2011, ApJ, 730, L35

Zheng W., Shu X., Moustakas J., Zitrin A., Ford H. C., Huang X., Broadhurst T., et al., 2014, ApJ, 795, 93

Zitrin A., Labbé I., Belli S., Bouwens R., Ellis R. S., Roberts-Borsani G., Stark D. P., Oesch P. A., Smit R., 2015, ApJ, 810, L12

Zitrin A., Meneghetti M., Umetsu K., Broadhurst T., Bartelmann M., Bouwens R., Bradley L., et al., 2013, ApJ, 762, L30

Table 5. Dropout galaxies; all confidence intervals are 68 per cent.

ID	$\alpha_{\rm J2000}$	$\delta_{\rm J2000}$	$m_{\rm F606W}$	$m_{\rm F814W}$	$m_{\rm F110W}$	$m_{\rm F140W}$	z^a	$P_7{}^b$	$P_8{}^b$	$P_9{}^b$
Dropouts with reliable photometry in all four bands										
EMACSJ1057-2261	$10^{\rm h}57^{\rm m}32.02^{\rm s}$	$57°59'30''$	>28.8	27.48 ± 0.69	26.04 ± 0.13	26.17 ± 0.20	$6.1^{+0.8}_{-1.0}$	0.19	0.01	0.00
EMACSJ1057-2279^c	$10^{\rm h}57^{\rm m}27.80^{\rm s}$	$57°59'7''$	>28.8	>28.4	25.15 ± 0.06	24.86 ± 0.06	$6.9^{+0.5}_{-0.3}$	0.79	0.14	0.00
EMACSJ1057-2476^c	$10^{\rm h}57^{\rm m}27.48^{\rm s}$	$57°59'7''$	>28.8	>28.4	24.55 ± 0.03	24.15 ± 0.03	$6.9^{+0.6}_{-0.1}$	0.74	0.25	0.00
MACSJ0140-0851	$1^{\rm h}39^{\rm m}58.63^{\rm s}$	$-5°56'12''$	>28.8	>28.4	25.13 ± 0.05	24.25 ± 0.03	$7.8^{+0.9}_{-0.2}$	0.19	0.60	0.17
MACSJ0140-1028	$1^{\rm h}40^{\rm m}3.70^{\rm s}$	$-5°55'15''$	>28.8	28.04 ± 0.97	26.38 ± 0.19	26.25 ± 0.24	$6.1^{+1.7}_{-1.8}$	0.19	0.09	0.01
MACSJ0152-0477	$1^{\rm h}52^{\rm m}33.16^{\rm s}$	$-28°54'42''$	>28.8	>28.4	26.62 ± 0.16	26.35 ± 0.17	$6.9^{+1.2}_{-1.4}$	0.32	0.17	0.01
MACSJ0152-0651	$1^{\rm h}52^{\rm m}34.36^{\rm s}$	$-28°54'27''$	>28.8	>28.4	25.89 ± 0.11	25.88 ± 0.16	$6.8^{+0.5}_{-0.4}$	0.67	0.07	0.00
MACSJ0152-0871	$1^{\rm h}52^{\rm m}36.05^{\rm s}$	$-28°54'35''$	>28.8	>28.4	22.76 ± 0.02	22.79 ± 0.03	$6.9^{+0.1}_{-0.0}$	1.00	0.00	0.00
MACSJ0257-0913	$2^{\rm h}57^{\rm m}41.18^{\rm s}$	$-22°10'10''$	>28.8	>28.4	26.23 ± 0.15	25.89 ± 0.14	$6.9^{+1.1}_{-0.9}$	0.37	0.23	0.01
MACSJ0712-0608	$7^{\rm h}12^{\rm m}13.17^{\rm s}$	$59°32'52''$	>28.8	>28.4	25.99 ± 0.10	25.58 ± 0.10	$7.0^{+1.0}_{-0.7}$	0.43	0.25	0.00
MACSJ0947-0072	$9^{\rm h}47^{\rm m}17.86^{\rm s}$	$76°24'21''$	>28.8	27.87 ± 1.37	24.62 ± 0.05	24.56 ± 0.07	$6.5^{+0.4}_{-0.3}$	0.53	0.00	0.00
MACSJ1115-0329	$11^{\rm h}15^{\rm m}15.94^{\rm s}$	$53°19'5''$	28.28 ± 0.84	>28.4	26.35 ± 0.18	26.34 ± 0.25	$6.8^{+1.1}_{-1.1}$	0.39	0.13	0.01
MACSJ1115-0632	$11^{\rm h}15^{\rm m}17.45^{\rm s}$	$53°20'27''$	28.65 ± 1.60	>28.4	25.23 ± 0.08	24.67 ± 0.07	$7.3^{+0.7}_{-0.7}$	0.48	0.39	0.01
MACSJ1124-0811	$11^{\rm h}24^{\rm m}28.77^{\rm s}$	$43°50'41''$	>28.8	>28.4	26.38 ± 0.17	25.89 ± 0.15	$7.1^{+1.3}_{-1.4}$	0.28	0.25	0.04
MACSJ1133-0922	$11^{\rm h}33^{\rm m}8.33^{\rm s}$	$50°8'27''$	28.63 ± 1.39	>28.4	25.98 ± 0.13	25.47 ± 0.12	$7.2^{+1.1}_{-1.0}$	0.35	0.29	0.02
MACSJ1621-0860	$16^{\rm h}21^{\rm m}23.01^{\rm s}$	$38°11'13''$	>28.8	>28.4	26.51 ± 0.13	26.22 ± 0.14	$6.8^{+1.1}_{-1.1}$	0.36	0.17	0.00
MACSJ1652-0135	$16^{\rm h}52^{\rm m}26.52^{\rm s}$	$55°34'43''$	>28.8	>28.4	26.81 ± 0.19	26.52 ± 0.20	$6.9^{+1.4}_{-1.9}$	0.26	0.17	0.02
MACSJ2051-0806	$20^{\rm h}51^{\rm m}13.80^{\rm s}$	$2°16'48''$	>28.8	>28.4	26.32 ± 0.16	26.11 ± 0.18	$6.9^{+1.1}_{-1.0}$	0.39	0.18	0.01
MACSJ2135-0509	$21^{\rm h}35^{\rm m}10.90^{\rm s}$	$-1°3'12''$	>28.8	>28.4	25.76 ± 0.14	25.52 ± 0.16	$6.9^{+0.9}_{-0.5}$	0.53	0.23	0.00
MACSJ2135-0763	$21^{\rm h}35^{\rm m}8.24^{\rm s}$	$-1°2'41''$	>28.8	27.80 ± 1.11	24.59 ± 0.04	23.36 ± 0.02	$9.1^{+0.3}_{-0.5}$	0.00	0.07	0.78
MACSJ2135-1078	$21^{\rm h}35^{\rm m}14.82^{\rm s}$	$-1°2'25''$	28.72 ± 2.05	>28.4	26.15 ± 0.18	25.69 ± 0.16	$7.2^{+1.2}_{-1.2}$	0.31	0.26	0.05
SMACSJ0600-0180	$6^{\rm h}0^{\rm m}9.21^{\rm s}$	$-43°53'6''$	>28.8	28.04 ± 1.19	25.48 ± 0.11	24.81 ± 0.08	$6.9^{+1.7}_{-1.0}$	0.27	0.26	0.03
SMACSJ0600-0427	$6^{\rm h}0^{\rm m}9.12^{\rm s}$	$-43°53'44''$	>28.8	28.33 ± 1.44	25.01 ± 0.07	24.06 ± 0.04	$8.0^{+0.9}_{-0.5}$	0.11	0.48	0.25
SMACSJ2031-0768	$20^{\rm h}31^{\rm m}45.98^{\rm s}$	$-40°37'31''$	>28.8	>28.4	26.38 ± 0.13	25.87 ± 0.11	$7.2^{+1.1}_{-1.3}$	0.30	0.25	0.02
SMACSJ2131-0444	$21^{\rm h}31^{\rm m}6.95^{\rm s}$	$-40°18'57''$	>28.8	>28.4	24.38 ± 0.04	24.33 ± 0.06	$6.9^{+0.2}_{-0.1}$	0.98	0.00	0.00
SMACSJ2131-0516	$21^{\rm h}31^{\rm m}6.47^{\rm s}$	$-40°18'51''$	>28.8	>28.4	25.07 ± 0.08	24.83 ± 0.09	$6.9^{+0.5}_{-0.2}$	0.78	0.16	0.00
SMACSJ2131-0567	$21^{\rm h}31^{\rm m}6.14^{\rm s}$	$-40°18'23''$	27.61 ± 0.91	>28.4	25.24 ± 0.09	24.45 ± 0.06	$7.5^{+1.1}_{-0.4}$	0.35	0.46	0.11
Summed probabilities for objects with reliable photometry in all four bands:								11.6	5.6	1.6
Dropouts with defective F110W photometry^d										
MACSJ0712-0414	$7^{\rm h}12^{\rm m}25.64^{\rm s}$	$59°31'55''$	>28.8	>28.4	—	22.72 ± 0.02	$8.2^{+1.8}_{-0.4}$	0.21	0.31	0.31
MACSJ0712-0699	$7^{\rm h}12^{\rm m}29.23^{\rm s}$	$59°32'59''$	>28.8	27.20 ± 1.55	—	23.69 ± 0.05	$6.5^{+2.0}_{-0.5}$	0.18	0.17	0.17
SMACSJ0549-0900	$5^{\rm h}49^{\rm m}16.25^{\rm s}$	$-62°5'15''$	>28.8	>28.4	—	24.35 ± 0.05	$8.0^{+1.9}_{-0.9}$	0.23	0.24	0.24
SMACSJ0549-1009	$5^{\rm h}49^{\rm m}14.87^{\rm s}$	$-62°5'46''$	>28.8	>28.4	—	23.68 ± 0.04	$7.9^{+2.0}_{-0.4}$	0.23	0.28	0.28
SMACSJ0549-9147	$5^{\rm h}49^{\rm m}11.29^{\rm s}$	$-62°5'7''$	28.56 ± 2.22	>28.4	—	24.62 ± 0.07	$7.9^{+2.1}_{-0.9}$	0.22	0.23	0.23
Summed probabilities for candidates with defective F110W photometry:^{e}								0.7	0.4	0.1
Net summed probability in each redshift bin:								12.2	5.9	1.7
Net detections reported in each redshift bin:								$\mathbf{12^{+4}_{-3}}$	$\mathbf{6^{+3}_{-2}}$	$\mathbf{2^{+2}_{-1}}$

^{a} 68 per cent confidence intervals.

^{b} P_7, P_8, and P_9 denote the probabilities that the object falls within redshift bins $[6.5, 7.5)$, $[7.5, 8.5)$, or $[8.5, 9.5)$, respectively.

^{c} Part of multiply-lensed system; see Section 6.

^{d} Reported probabilities for dropouts with defective F110W photometry are those derived directly from the BPZ fit, before application of a prior based on the redshifts of the other dropouts (see text).

^{e} Summed probabilities reflect the prior described in the text and referenced in the immediately preceding note.